Assessment of phase change materials for thermal energy storage in battery systems for heavy-duty vehicle applications

Energy Conversion and Management 349 (2026) 120816

Contents lists available at ScienceDirect

Energy Conversion and Management

journal homepage: www.elsevier.com/locate/enconman

Assessment of phase change materials for thermal energy storage in battery systems for heavy-duty vehicle applications

Elisa Revello [a], Prakhar Dixit [b], Konsta Turunen [b], Annukka Santasalo-Aarnio [b], Alessandro Hugo Antonio Monteverde [a,*]

[a] Politecnico di Torino, Department of Applied Science and Technology, Corso Duca degli Abbruzzi, 24, 10129 Torino, Italy
[b] Aalto University, Department of Energy and Mechanical Engineering, Research group of Energy Conversion and Systems, Otakaari 4, 00076, Finland

ARTICLE INFO

Keywords:
Phase change materials
Thermal characterization
Hybrid heat dissipation
Thermal management
Lithium-ion batteries

ABSTRACT

Thermal management plays a crucial role in ensuring performance, safety, and durability in heavy-duty vehicles (HDVs), particularly under demanding operating conditions. This study investigates the use of phase change materials (PCMs) for passive thermal control, focusing on the thermal characterization and performance evaluation of commercial PCMs for battery thermal management systems (BTMS). Differential scanning calorimetry (DSC) identified n-octadecane as the most promising candidate, with a melting range of 25–32 °C, a latent heat of fusion of 222.2 J g^{-1}, and good thermal stability. Experimental tests in a dedicated thermal energy storage (TES) system examined the charging and discharging behaviour of n-octadecane under varying heat transfer fluid (HTF) flow rates. The heat transfer was conduction-dominated in the solid state and convection-enhanced in the liquid state. Increasing the heat transfer fluid (HTF) flow rate had limited influence on charging/discharging time but improved thermal power ratio of the TES to 56 at 3 L min^{-1}, representing a 3.5-fold improvement over the baseline configuration without PCM. Experimental results highlighted that incorporating PCM into the TES system increased the gravimetric specific power to 0.056 kW kg^{-1} – 3.5 times higher than the baseline configuration without PCM (0.016 kW kg^{-1}). Additionally, the volumetric specific power reached approximately 68 kW m^{-3}, a sixfold enhancement compared to the baseline. These findings support the design of modular PCM-integrated TES systems as scalable solutions for HDV battery pack cooling or cabin thermal management.

1. Introduction

Nowadays, the depletion of fossil fuel resources and climate change emerge as the most critical challenges, particularly within the transportation sector, which constitutes a significant share of total energy consumption [1,2,3]. Although they represent fewer than 8 % of vehicles, heavy-duty vehicles (HDVs) are responsible for more than 35 % of direct CO_2 emissions from road transport. To align with the net zero emissions by 2050 (NZE) scenario, is essential to achieving the 15 % emission reduction target by 2030, declining at roughly 2 % per year [3–6].

The integration of rechargeable batteries in electric vehicles (EVs) has increased markedly in recent years. Particularly, lithium-ion batteries (LiBs) are increasingly favoured for EV applications due to their high energy density, long lifespan, efficiency and scalability [7–9]. A lifespan of 10 to 15 years is a critical requirement for LiBs that are targeted for EVs [7,10].

HDVs such as buses operate under high power loads, often in harsh environments with limited opportunities for passive cooling. Hybrid EVs require highly integrated and advanced thermal management system (TMS) due to the thermal sensitivity of multiple subsystems (e.g. engine, passenger cabin, battery pack, electric motor, and power electronics). Among these, cabin conditioning and battery thermal management system (BTMS) are critical [8].

The thermal management of electrified vehicles has been extensively examined in the literature. As discussed in the previous paragraph, until significant advancements in battery technology occur, the performance of current EV batteries rely heavily on the effectiveness of BTMS. Based on numerous scientific studies, the optimal operating temperature range for LiBs spans from 20 °C to 40 °C while the optimum temperature is approximately 30 °C [2]. To prevent non-uniform thermal distribution and potential runaway reactions, the internal temperature gradient across individual cells and battery components should be maintained below 5 °C [9,11].

Currently, BTMS are broadly classified into three categories: passive,

* Corresponding author.
E-mail address: alessandro.monteverdevidela@polito.it (A.H.A. Monteverde).

https://doi.org/10.1016/j.enconman.2025.120816
Received 22 July 2025; Received in revised form 15 November 2025; Accepted 22 November 2025
Available online 30 November 2025

Nomenclature

Acronyms

ASTM	American society for testing and materials
BTMS	Battery thermal management system
DSC	Differential scanning calorimetry
EV	Electric vehicle
HDV	Heavy-duty vehicle
HTF	Heat transfer fluid
LiB	Lithium-ion battery
MTPS	Modified transient plane source
NZE	Net zero emissions
PCM	Phase change material
TES	Thermal energy storage
TMS	Thermal management system

Symbol

$\dot{m}_{HTF}$	Mass flow rate of HTF, kg s^{-1}
H_m	Latent heat of melting, J g^{-1}
H_s	Latent heat of solidification, J g^{-1}
$P_{charging}$	Mean power of charging, kW
$P_{discharging}$	Mean power of discharging, kW
T_h	DSC heating temperature, °C
$T_{HTF,in}$	HTF inlet temperature, °C
$T_{HTF,out}$	HTF outlet temperature, °C
T_{PCM}	PCM mid-point bottom temperature sensor, °C
T_c	DSC cooling temperature, °C
$T_{m/onset}$	Onset temperature of melting, °C
$T_{m/peak}$	Peak temperature of melting, °C
$T_{s/onset}$	Onset temperature of solidification, °C
$T_{s/peak}$	Peak temperature of solidification, °C
$\dot{V}$	Volumetric flow rate of HTF, L min^{-1}
$c_{p,i}$	Specific heat capacity of i, J (g^{-1} K^{-1})
$t_{charging}$	Time of charging, s
$t_{discharging}$	Time of discharging, s
η_{TES}	PCM-based TES thermal power ratio
ρ_{HTF}	Density of HTF, kg m^{-3}
Δt	Time interval between two consecutive readings, s

active, and hybrid. Active systems utilize externally powered devices (such as pumps, fans, or compressors) to circulate a coolant (e.g., air, liquid, or refrigerant), facilitating controlled heat removal from the battery pack. Conversely, passive BTMSs are simpler and more cost-effective since they operate without external energy input, relying on natural convection, conduction, or phase change mechanisms for thermal regulation. Hybrid BTMS emerges as a pivotal solution to strike a balance between advantages of passive and active cooling systems, aiming to optimize thermal performance by balancing energy efficiency and temperature uniformity across a wide range of operating scenarios [12–14].

Phase change materials (PCMs) emerged as a viable strategy, owing to their ability to absorb and release latent heat during solid–liquid transition. This enables passive and energy-efficient temperature regulation under thermal spikes. PCMs have been extensively utilized in various thermal management applications, including buildings [15] and refrigeration systems, where they contribute to improved energy efficiency and reduced operational costs. Nevertheless, the widespread adoption of PCMs in EV battery systems is still constrained by their inherently low thermal conductivity (typically between 0.2 and 2 W m^{-1} K^{-1}) and the complex design requirements needed for effective integration into thermal management architectures. This following paragraph summarizes the most relevant research focused on TM in electric buses using a thermal energy storage (TES) system with PCM.

Knote et al. [12] conducted a detailed assessment of bus energy consumption as a function of ambient temperature. According to their findings, the specific energy consumption of an articulated bus operating at ambient temperatures between − 5 °C and 0 °C reached approximately 3.0 kWh km^{-1}, while at 15–25 °C, it decreased to about 1.5 kWh km^{-1}. Similarly, for a standard 12-meter bus, the energy consumption was around 2.7 kWh km^{-1} at − 5 to 0 °C, decreasing to approximately 1.3 kWh km^{-1} under milder conditions. These results clearly demonstrated that operating in sub-zero conditions nearly doubles the vehicle's energy demand per kilometer, largely due to increased thermal loads for cabin heating and reduced system efficiency. Kuitunen et al. [13,14] proposed a high-speed charging TES system employing paraffin-based phase change material for thermal regulation in urban electric buses. Designed to maintain cabin temperature near 18 °C, the system achieved full thermal charge within minutes via a high-voltage terminal charger. Another study highlighted the operational impact of a 12-meter electric bus with a nominal battery capacity of 300 kWh. Under diesel-assisted heating, the expected driving range varied between 214 km and 300 km, depending on conditions, whereas under full electric heating, the range is significantly reduced to approximately 130 km. The authors underscored the critical influence of thermal management strategies on the energy efficiency and operational range of battery-electric buses, particularly under cold ambient conditions [16]. Kraft et al. [17] emphasized the two primary charging strategies commonly implemented for electric city buses. The first is the opportunity charging approach, wherein the vehicle undergoes frequent high-power charging sessions at designated points such as terminals and depots throughout the day. The second is the overnight charging strategy, where the bus is recharged exclusively during extended downtime at the depot after completing its daily operation. Considering the night charging scenario, where continuous electrical heating was expected without intermediate energy replenishment, TES systems must exhibit gravimetric energy densities exceeding 169 Wh kg^{-1} to provide sufficient thermal buffering over a full duty cycle. Wang et al. [18] designed and tested a thermal storage system for EV cabin heating, incorporating a PCM-based heat exchanger. Their analysis, using MATLAB Simulink simulations, evaluated the system's performance in maintaining desired cabin temperatures for approximately 46 min, aligning with typical daily commutes, and optimizing energy consumption. Hossan et al. [19] developed a 1/20th prototype bus model to experimentally investigate thermal behaviour of the bus under traffic. Sodium sulphate decahydrate was employed as the PCM on the roof. Experimental analysis indicated that integrating a PCM layer on the roof and thermally shielding the heat source significantly attenuated internal temperature rise and reduced temporal temperature fluctuations. In open conditions, the mean interior temperature was maintained approximately 4.22 °C below ambient, with a maximum differential of 7.5 °C. Pra et al. [20] experimentally and numerically assessed the hybrid TMS for an electric van's battery pack, combining PCM- expanded graphite matrix with active air cooling. Results indicated that, starting from an initial cell temperature of 40 °C, the battery pack temperature remained below 40 °C throughout the mission when cooled by 2.5 m s^{-1} airflow at 30 °C. Moreover, extensive experimental and numerical investigations have been conducted to evaluate the effectiveness of incorporating expanded graphite, aluminum foam, and heat dissipation fins in enhancing the thermal conductivity of PCMs in direct thermal contact with individual battery cells [21–26].

Based on the literature review, significant progress has been made in PCM-based BTM systems; however, most studies remain limited to small-scale battery modules or passenger EVs with critical challenges –

such as low thermal conductivity, cycling stability, re-solidification time, encapsulation/leakage, safety, and the absence of standardized test protocols for pack-level aging and TES integration – still unresolved for large battery packs [24,25]. Current research is heavily skewed toward numerical simulations, with little experimental validation under realistic thermal loading conditions. A critical gap lies in PCM selection, which is often guided by manufacturer-reported or nominal thermal property values and rarely includes cyclic thermal durability testing – essential for vehicle applications involving frequent charge–discharge cycles [26,27]. PCMs often suffer latent capacity loss, subcooling, or phase segregation after extended cycling, but the underlying chemical, mechanical, and microstructural degradation pathways under realistic pack conditions remain insufficiently understood. Additionally, the influence of flow-dependent thermal parameters, such as variations in heat transfer fluid (HTF) volume flow rates on charging/discharging power output and TES efficiency, has received limited attention [28]. Practical performance metrics, including gravimetric and volumetric specific power, are frequently overlooked. To bridge these gaps, this work first examines the most suitable PCM for BTMS of HDVs. Five commercial PCMs were assessed through comprehensive thermal characterization. Critical thermophysical properties, including the onset and peak temperatures of melting and solidification, as well as the phase transition enthalpy, were systematically evaluated. Furthermore, thermal cycling tests have been conducted to evaluate the long-term thermal stability and durability of the PCMs under repeated phase change conditions. Based on the outcomes of the thermal characterization, the performance of n-octadecane was experimentally assessed in a dedicated TES setup. Various HTF volume flow rates were tested to determine their effect on the mean thermal power exchanged by the PCM during melting and solidification. Additionally, charging and discharging times of the n-octadecane were evaluated. Overall, the novelty of this study lies in the experimental validation of a PCM-based TMS through combined cyclic durability testing and system-level assessment of gravimetric and volumetric specific power, thereby establishing a system-level framework tailored to the stringent thermal and operational requirements of HDVs batteries.

2. Materials and methods

2.1. Materials

In this study, five commercial PCMs namely n-octadecane, lauric acid, stearic acid (supplied by Thermo Scientific), n-eicosane and paraffin 52–54 °C (provided by Merck) were selected to assess their thermal performance to identify the most suitable PCM for BTM. Table 1 detailed the specific information provided by the manufacturer of the PCMs. The five PCMs were chosen to span a range of phase change temperatures, allowing evaluation under different operational conditions, while exhibiting sufficient thermal capacity for effective energy storage. Durability and cycling stability were also considered to minimize degradation, phase separation, or supercooling during repeated melting and solidification. Additionally, material compatibility with common heat exchanger metals and considerations of toxicity and safety were also considered to ensure safe handling and potential practical applicability. These factors ensure that the chosen PCMs are representative of materials that balance performance, stability, operational relevance, and safe handling.

Table 1
Specific properties of chosen PCMs (Information provided by the manufacturer and literature).

Description	N-octadecane	N-eicosane	Lauric acid	Paraffin 52–54 °C	Stearic acid
Formula	$C_{18}H_{38}$	$C_{20}H_{42}$	$C_{12}H_{24}O_2$	n.a.	$C_{18}H_{36}O_2$
Purity	90 %	n.a.	≥ 98 %	n.a.	97 %
Molecular weight	254.5 g mol^{-1}	282.56 g mol^{-1}	200.32 g mol^{-1}	n.a.	284.47 g mol^{-1}
Melting range	27 – 32 °C	35 – 40 °C	43 – 48 °C	51 – 56 °C	66 – 71 °C
Flash point	166 °C	176 °C	156 °C	>100 °C	196 °C
Latent heat	240 J g^{-1} [29]	243 J g^{-1} [30]	185 J g^{-1} [31]	210 J g^{-1} [32]	220 J g^{-1} [33]
Density	777 kg m^{-3}	789 kg m^{-3}	883 kg m^{-3}	766 kg m^{-3}	840 kg m^{-3}
Water solubility	Insoluble	Insoluble	Insoluble	n.a.	Slightly soluble

2.2. Thermophysical properties

2.2.1. Differential scanning calorimetry (DSC)

Thermal properties of the selected PCMs (Table 1) were measured using differential scanning calorimetry (DSC) on a Netzsch DSC204F1 Phoenix DSC instrument. Nitrogen (20 L min^{-1}) was employed both as a purging and protection gas [34]. Before setting the temperature program, a temperature and sensitivity calibration on the DSC instrument with a reference material must be performed. The heat flow curve was recorded within a temperature range from −20 °C to 95 °C to cover the phase transition interval of the selected materials. The first step was at a constant temperature of 25 °C for 5 min, then a dynamic step heated the sample up to the heating temperature (T_h), followed by an isotherm at T_h for 2 min, subsequently a cooling step to the cooling set temperature (T_c) and finally maintaining the temperature constant at T_c for 5 min. In each test, the first set of recorded data was discarded, as it was susceptible to the thermal history of the instrument. The PCMs samples weighted from 10 mg to 20 mg were exposed to the dynamic DSC program to record the heat flow rate in the sample as a function of temperature, thus obtaining the DSC curve. Thermal cycling was performed at rates spanning from 1 to 10 K min^{-1}. The measurement of the sample masses was carried out on Precisa 3100C bilance with a readability of 0.01 g. For each test, the heating–cooling program was repeated at least twice to ensure reproducibility. Several experimental parameters, such as sample mass, scanning rate, atmospheric flow, thermal resistance between the DSC measurement sensor and the sample crucible, as well as calibration and measurement method, or external conditions may affect the results of thermal properties obtained from a DSC test [35]. This work examined the influence of changing the sample mass and scanning rate (reported in the Supporting Information) by comparing the DSC results of thermal properties of the PCMs listed in Table 1. The onset temperature (T_{onset}) corresponds to the beginning of the endothermic/exothermic peak and it can be estimated as the intersection between the tangent of the maximum point of the front slope of the peak on the DSC curve and the baseline. The endothermic/exothermic peak temperature (T_{peak}) is at the maximum heat flow. According to national standards, in this study, the melting/solidification temperature was attributed to the endothermic or exothermic peak temperature ($T_{m/peak}$ or $T_{s/peak}$, respectively) and the latent heat of melting/solidification ($H_{m/s}$) has been determined as the area under the endothermic/exothermic peak. Moreover, the thermal stability of each sample of PCM was examined over 20-consecutive cycles through the DSC instrument.

The specific heat capacity (C_p) of a PCM is a crucial property to consider when determining its functionality in certain applications. In this study, the C_p measurement was carried out on the DSC (with the temperature program previously described) using the sapphire correction method established by the American Society for Testing and Materials (ASTM). Particularly, this method estimates the unknown specific heat capacity of a sample by analysing the difference in heat flow between a reference material with a well-known heat capacity and the sample under investigation.

2.2.2. Thermal conductivity measurement

The thermal conductivity was measured on a C-Therm thermal conductivity analyzer (C-Therm TCi) with an accuracy better than 5 %

and precision better than 1 %. This method employs the modified transient plane source (MTPS) technique. During measurement, a low-power, short-duration electrical current is applied to the sensor's heating element, inducing a transient temperature rise at the sensor–sample interface. The resulting thermal response is monitored by measuring changes in the voltage signal, which is influenced by the thermal dissipation characteristics of the sample. The slope of the voltage vs. time curve is directly correlated to the sample's thermal conductivity. Particularly, the thermal conductivity of the sample is inversely proportional to the rate of increase in sensor voltage. This technique allows for rapid and non-destructive testing of a wide range of materials, including solids and liquids. The sample prepared for thermal conductivity measurement in solid state weighted approximately 12 g, it has a diameter of 30 mm, and it has been polished to obtain as much as possible a flat and smooth surface. Moreover, water was used as a contact liquid between the solid sample and the sensor.

2.2.3. Thermogravimetric analysis (TGA)

Thermogravimetric analysis (TGA) was conducted using Netzsch STA 449 F3 Jupiter to further assess the thermal stability of the material. A sample of approximately 6 mg was heated from 25 °C to 375 °C at a rate of 10 °C/min under a nitrogen atmosphere (50 L min^{-1}).

2.3. Thermal boundaries and experimental setup

To accurately evaluate the thermal performance of the proposed BTMS under conditions representative of HDV operation, the temperature boundaries and experimental setup were defined based on literature data and realistic high-rate cycling profiles.

2.3.1. Definition of operating temperature range for HDV-oriented BTMS

Based on extrapolated data from literature [36], Fig. S.12 (reported in the Supporting Information) evidence the temperature profile of a commercial prismatic LiB modules (3.2 V/8 Ah) at a 3C discharge/1C charge cycle. The temperature profile of the baseline module (battery without PCM) provides a crucial experimental benchmark that reveals the intrinsic thermal limitations of conventional air-cooled systems, particularly under the high discharge rates representative of HDV operation. As shown in Fig. S.12, the battery temperature rises sharply from approximately 25 °C to 45 °C during each 3C discharge period and does not return to its initial level during subsequent 1C charging. This cyclical thermal accumulation demonstrates that the convective heat transfer coefficient of air (typically < 10 W m^{-2} K^{-1}) is insufficient to maintain thermal equilibrium, leading to a residual heat build-up of nearly 2–3 °C after every cycle. Such behaviour indicates a positive thermal drift, which, in extended operation, could result in uncontrolled temperature escalation beyond the safe limit of 50 °C, accelerating degradation and posing a thermal runaway risk. From an energy balance standpoint, approximately 22 kJ of heat is generated per discharge–charge cycle, of which only ~ 70 % is dissipated by air convection, while ~ 6 kJ remains stored in the cell as sensible heat ($\Delta T \approx$ 20 °C). This residual heat accumulation quantitatively confirms the thermal insufficiency of air-based cooling, especially for large-format cells or densely packed modules used in commercial EVs and HDVs where convective dissipation is further hindered by packaging constraints. These findings substantiate the need for an enhanced passive thermal management strategy, such as integrating a phase change material to achieve dynamic thermal equilibrium and suppress cumulative heating during repetitive high rate cycling. In our study, n-octadecane acts as a latent heat reservoir, absorbing excess heat near its melting temperature range (≈ 25–31 °C) and releasing it gradually during the subsequent charge phase. This mechanism introduces isothermal regulation, effectively flattening the temperature oscillations observed in the baseline configuration (Fig. S.12) and ensuring that the cell temperature remains within the optimal 30–35 °C window.

2.3.2. Experimental configuration

The performance of n-octadecane was experimentally assessed through the in-house built facility. The setup includes the TES tank with PCM, a water pump, a heater, a heat sink, a frequency converter, a PID controller, a data logger for the thermocouples and a data acquisition system to monitor the temperature distribution inside the TES tank (Fig. 1). The main dimensions of the TES device are summarized in Table 2. The fin and tube heat exchanger consisted of 18 copper tubes and 71 aluminium fins enclosed inside a rectangular container made of steel. In addition, two layers of polystyrene (20 mm thick) and one layer made of self-adhesive foam (10 mm thick) were added to reduce the heat loss of the TES system to the surroundings environment. The total heat transfer surface area was approximately 0.11 m^2. N-octadecane was introduced into the storage unit, occupying the interstitial volume between the aluminium fins and copper tubes. The PCM filled the region up to approximately the full height of the fins' upper edge, resulting in a total volumetric occupancy of 2.51 L.

The charge of the TES unit was controlled with a centrifugal pump (250 W), where circulated water. The HTF was heated using an electric heater (500 W) and cooled with a heat sink connected to the tap water system. Water inlet temperature to the storage unit was adjusted using a PID controller. Furthermore, HTF inlet and outlet temperature, PCM temperature at different locations were acquired with K-type thermocouples (accuracy of reading ± 0.5 °C). The temperature measurements of all the temperature sensors were recorded every 10 s by the data acquisition system. Particularly, seven temperature sensors were placed at different spots in the TES unit to measure the temperature of the confined PCM, as schematized in Fig. 2. The first two thermocouples measured the HTF temperature at the inlet (T1) and outlet (T2) sections of the TES unit (Fig. 2.a). Five thermocouples (from T3 to T7) were evenly distributed and spaced in the central region at 30 mm from the top of the TES (Fig. 2.b). This arrangement was specifically designed to monitor the spatial progression of the melting and solidification fronts along the main flow path, starting from the inlet side of the heat exchanger (T3) and extending toward the outlet section (T7). An additional thermocouple (T8) was in the middle, close to the bottom part of the tank (55 mm depth from the top) and the last one (T9) was placed in the middle near the top of the tank (5 mm from the top). Together, this configuration provided a comprehensive mapping of the temperature distribution across different vertical and horizontal regions of the TES, enabling a detailed assessment of phase change dynamics throughout the charging and discharging processes. Moreover, to control and maintain the desired temperature of the TES system during the charging/discharging tests, the setup was placed inside a refrigeration chamber.

2.4. Measurement procedure

2.4.1. Charging and discharging cycles

The experiment procedure for testing n-octadecane in the TES system consist of two stages: charging (melting the PCM by hot water) and discharging (solidifying the PCM by cold water). Data were recorded starting from the set point temperature of 15 ± 1 °C, then the HTF was pumped at different volume flow rates 2 L min^{-1}, 2.5 L min^{-1} and 3 L min^{-1} (changing the frequency converter) through the tube side of the TES tank to heat the PCM. During the charging phase, the n-octadecane underwent a solid-to-liquid state transition as its temperature increased from 15 ± 1 °C to 35 ± 1 °C. Upon complete melting of the PCM, the system was switched to cooling (discharging) mode, opening the cold tap water. In this phase, the PCM was thermally cycled back to its initial temperature, decreasing from 35 ± 1 °C to 15 ± 1 °C. Discharging cycles commenced immediately after the completion of charging cycles to exploit the thermal condition wherein the PCM remained in a fully liquefied state at approximately 35 ± 1 °C, thereby ensuring optimal thermal discharge efficiency. In addition, the experiments were carried out at the same time on subsequent days to ensure approximately

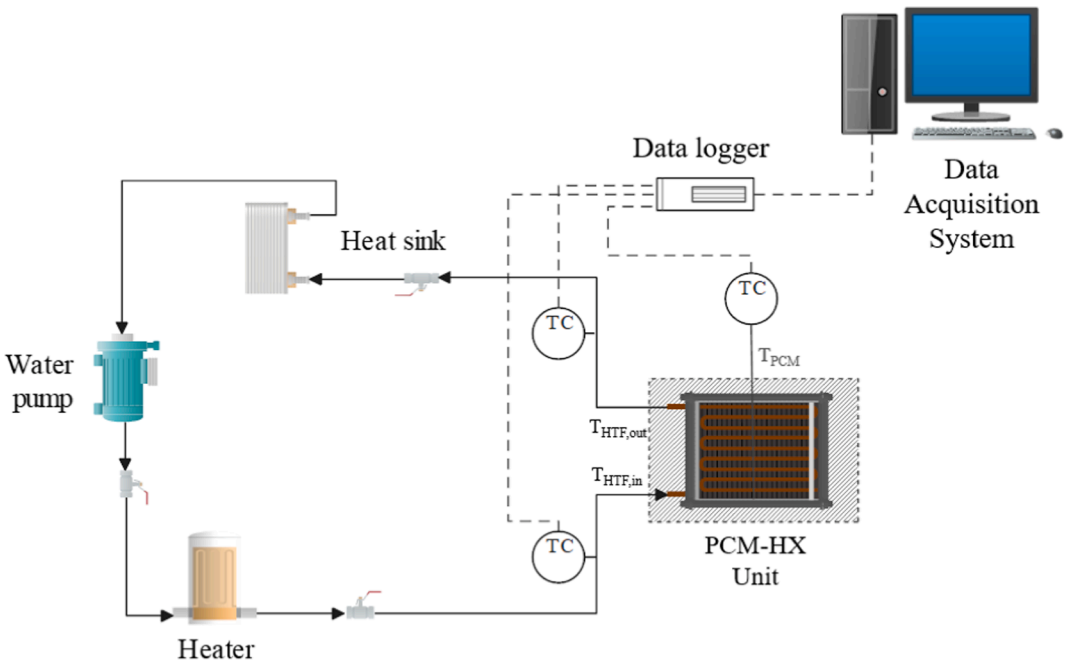

Fig. 1. Schematic representation of the experimental setup with the insulated fin and tube heat exchanger filled with PCM.

Table 2
The main dimensions of the TES tank and PCM filled within the TES unit.

Description	TES system	Unit
Casing material	Steel	_
Casing dimensions	232 × 263 × 58	mm
Casing mass	1.44	kg
Heat exchanger mass	0.85	kg
Aluminium plate thickness	1.3	mm
Aluminium plate length	230	mm
Aluminium fin thickness	0.1	mm
Aluminium fin height	44	mm
Fin spacing	3.0	mm
Copper tube length	240	mm
Copper tube diameter	7	mm
Insulation material	Polystyrene foam, self-adhesive foam	_
Insulation thickness	50	mm
	PCM	
Type	N-octadecane	_
Volume (liquid state)	2.51	L
Mass	1.96	kg

identical ambient conditions in all the tests. Each charging/discharging test was repeated three times for uncertainty analysis in order to ensure reliability.

2.4.2. Mean power and thermal power ratio of the TES

The mean thermal power output of the TES tank during both charging ($P_{charging}$) and discharging ($P_{discharging}$) phases was calculated using the following analytical expression.

$$P_{charging} = \frac{\sum_{T_{PCM}=15^{\circ}C}^{T_{PCM}=27^{\circ}C} \dot{m}_{HTF} C_{p,HTF} \left(T_{HTF,in} - T_{HTF,out}\right) \Delta t}{t_{charging}} \quad (1)$$

$$P_{discharging} = \frac{\sum_{T_{PCM}=34^{\circ}C}^{T_{PCM}=15^{\circ}C} \dot{m}_{HTF} C_{p,HTF} \left(T_{HTF,in} - T_{HTF,out}\right) \Delta t}{t_{discharging}} \quad (2)$$

T_{PCM} denotes the mid-point bottom temperature sensor of the PCM (T8), $T_{HTF,in}$ and $T_{HTF,out}$ are the inlet and outlet temperatures of the HTF during successive charging and discharging cycles. $\Delta t = 10$ s is the time step adopted in throughout this work. $t_{charging}$ is the time interval during which the temperature of the PCM increases from 15 °C to 27 °C.

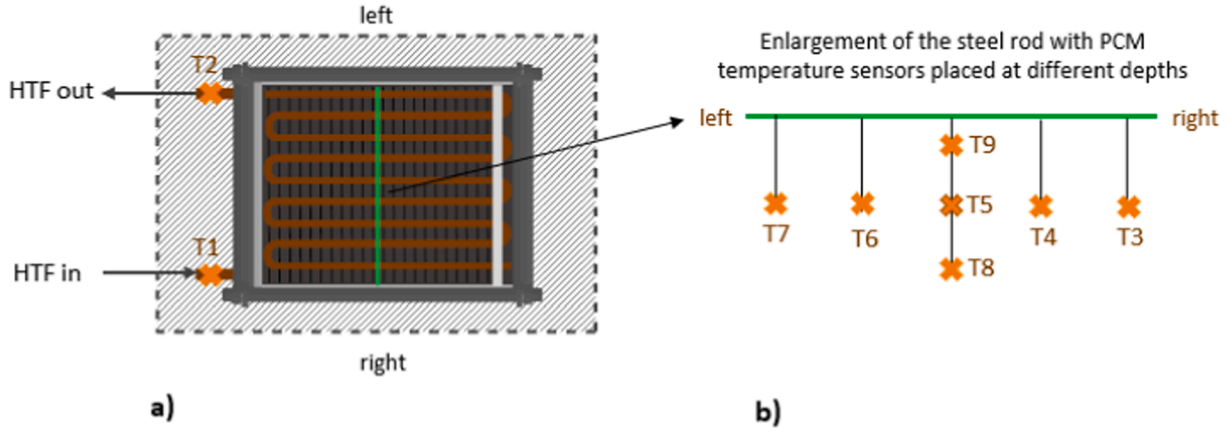

Fig. 2. (a) Top view of the temperature sensors; HTF inlet (T1) and HTF outlet (T2) temperature. (b) Front view of the PCM temperature sensors at different depth; 30 mm from the top (T3 to T7), 55 mm from the top (T8) and 5 mm from the top (T9).

Conversely, $t_{discharging}$ represents the duration required for the PCM to cool from 34 °C to 15 °C. The temperature boundaries were selected based on the thermal transition behaviour observed in the heat flow curve generated by the DSC. To ensure complete melting and solidification of the PCM, a minimum margin of at least ± 3.5 °C from the onset temperature recorded by the T8 sensor was applied in this study. $\dot{m}_{HTF}$ corresponds to the mass flow rate of the water which depends on the constant volumetric flow rate ($\dot{V}$) which is regulated through a frequency converter, and density (ρ_{HTF}) according to the following formula:

$$\dot{m}_{HTF} = \rho_{HTF}(T_{HTF,in}) \bullet \dot{V} \tag{3}$$

Where the density of the HTF is calculated as a function of the inlet with the expression [37]:

$$\rho_{HTF}(T_{HTF,in}) = -3.60e^{-3} \bullet T_{HTF,in}^2 - 6.61e^{-2} \bullet T_{HTF,in} + 1.0e^{3} \tag{4}$$

Lastly, $C_{p,HTF}$ is the specific heat capacity of the HTF determined using the following expression [38]:

$$C_{p,HTF}(T_{HTF}) = 2.84e^{-9} \bullet T_{HTF}^4 - 7.15e^{-7} \bullet T_{HTF}^3 + 7.21e^{-5} \bullet T_{HTF}^2 - 2.93e^{-3} \bullet T_{HTF} + 4.22 \tag{5}$$

Accordingly, the thermal power ratio (η_{TES}) of the PCM-based TES system was evaluated as a dimensionless indicator of dynamic balance between PCM charging and discharging rates. η_{TES} is the ratio between the thermal power absorbed during the charging phase and the thermal power released during the discharging phase:

$$\eta_{TES} = \frac{P_{discharging}}{P_{charging}} \tag{6}$$

Therefore, this index reflects the capability of a PCM-based TES system to buffer transient thermal loads during charging and to efficiently release the stored energy during discharging, thereby ensuring readiness for subsequent cycles — a critical aspect in HDV BTMS applications characterized by frequent load fluctuations.

3. Results and discussion

3.1. Thermal characterization of individual PCMs

This section presents the primary outcomes of the thermal characterization of the five commercial PCMs.

Fig. 3 and Fig. 4 encompassed the thermal properties results from DSC tests carried out at 5 K min^{-1} emphasizing a clear distinction in the melting and solidification behaviour of various PCMs. Fig. 3 depicted the onset and peak temperature associated with both the melting and solidification transitions for the five PCMs under investigation. Correspondingly, Fig. 4 reported the measured latent heat of fusion and crystallization. Particularly, n-octadecane, n-eicosane and paraffin 52–54 °C are three organic paraffins (C_nH_{2n+2}) which are saturated hydrocarbons with similar properties. Melting/Solidification point, and latent heat generally exhibited an increasing trend with chain length, potentially leading to multiple transition peaks may occur [39]. Conversely, lauric acid and stearic acid are fatty acids ($C_nH_{2n+1}COOH$) which melted over a wide range of temperature and have a large variation in latent heat of fusion [40]. Overall, the melting and solidification points obtained were consistent with the value reported by the manufacturer (Table 1). Among the tested PCMs, n-octadecane, n-eicosane and stearic acid exhibited the highest latent heat values. The measured enthalpies of fusion were approximately 222 J g^{-1}, 253 J g^{-1}, and 224 J g^{-1}, respectively, while the corresponding enthalpies of solidification were 218 J g^{-1}, 250 J g^{-1}, and 223 J g^{-1}. These values reflected their excellent capacity to store and release energy upon phase transition, corroborating previous literature data [40–45].

Fig. 5 summarizes the thermal cycling tests at 5 K min^{-1} rate for each PCM, highlighting the enthalpy values after the first and twentieth cycles. Among paraffins, n-octadecane retained consistent thermal performance over 20 melting/solidification cycles, with enthalpy degradation under 1 %, in accordance with the conclusions reached by Zhang et al. [46]. This level of repeatability confirms its thermal reliability and long-term usability under repeated charging and discharging operations, essential characteristics for HDVs applications. N-eicosane, lauric acid and paraffin 52–54 °C exhibited moderate stability, with small but noticeable shifts in enthalpies values across multiple cycles.

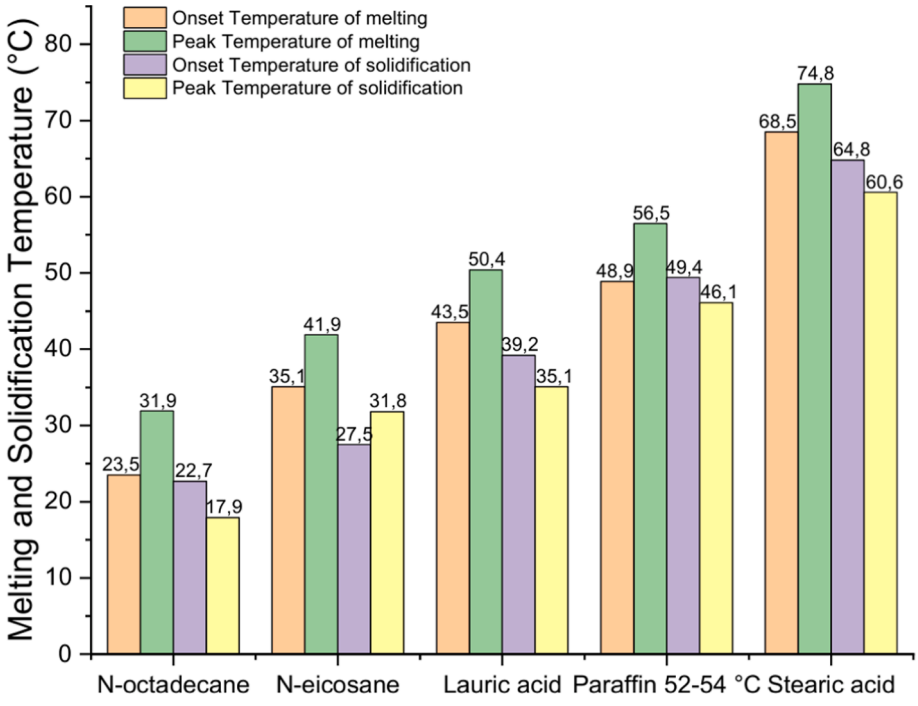

Fig. 3. Melting and solidification temperature of the selected PCMs.

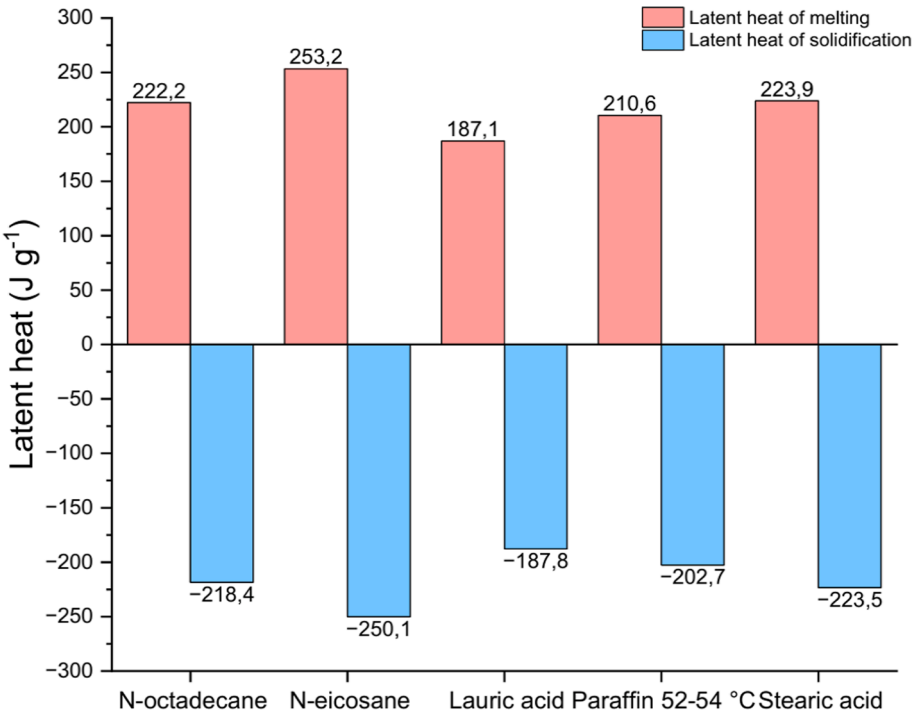

Fig. 4. Latent heat of melting and solidification of the selected PCMs.

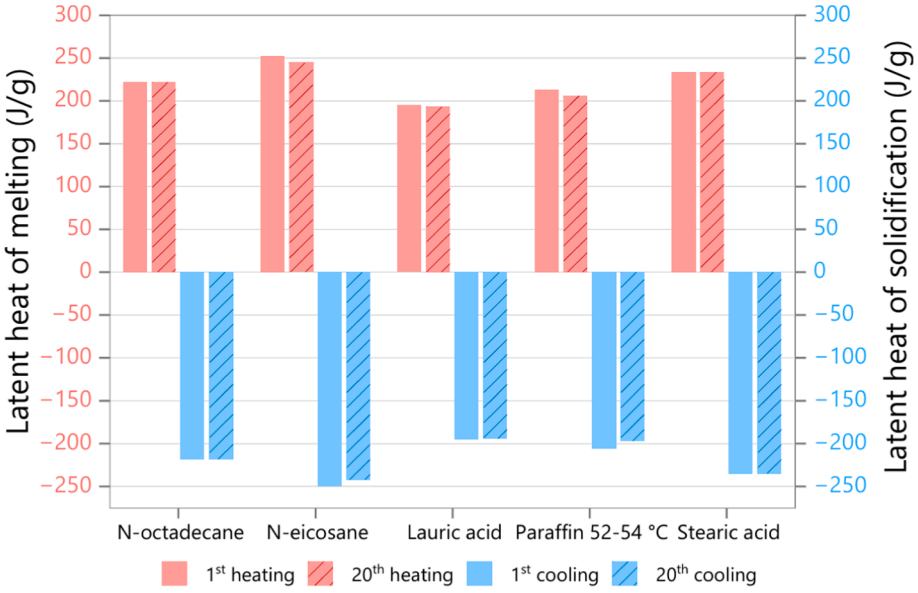

Fig. 5. Latent heat of melting and solidification of PCMs after one cycle and after twenty thermal cycles.

Lastly, among the fatty acids, stearic acid demonstrated good long-term cyclic stability with minimal variation in enthalpies values, which is aligned with the findings reported by Xu and Yang [47].

In addition, Table 3 presented the specific heat capacities determined through DSC analysis for each PCM. Generally, PCMs have a higher specific heat in the liquid state due to increased molecular mobility. In the solid state, molecular motion is predominantly confined to vibrational modes within a well-ordered lattice. Upon transitioning to the liquid state, the system gains additional translational and rotational degrees of freedom, thereby increasing the number of accessible microstates [34].

Based on the outcomes achieved, n-octadecane demonstrated strong potential as a candidate for passive thermal management in battery

Table 3
Specific heat capacity measured from DSC analysis of each PCMs.

Property	N-octadecane	N-eicosane	Lauric acid	Paraffin 52–54 °C	Stearic acid	Unit
$C_{p,PCM}(s)$	1.61 (@ −14.5 °C)	1.66 (@ 0 °C)	2.15 (@ 25.5 °C)	1.62 (@ −10 °C)	1.78 (@ 25 °C)	J (g^{-1} K^{-1})
$C_{p,PCM}(l)$	2.09 (@ 50C°)	2.27 (@ 50 °C)	2.25 (@ 60 °C)	2.14 (@ 65 °C)	2.34 (@ 85 °C)	J (g^{-1} K^{-1})

systems. Its high enthalpy of fusion (222 J g^{-1}) enables the material to absorb and store a significant amount of thermal energy during phase transition, which is crucial for effectively suppressing temperature spikes in LiB. With a melting point in the desirable range of 30–35 °C, n-octadecane is best suited for moderate or cooler climates where ambient temperatures enable repeated solid–liquid cycling. In contrast, in persistently warm climates where temperatures remain above its melting point, the lack of resolidification limits its long-term thermal storage capacity. This range closely matches the upper limit of the optimal operating window of LiB, meaning the PCM begins to absorb heat precisely when the battery temperature approaches conditions that could accelerate degradation or cause safety risks, maximizing cooling efficiency – avoiding unnecessary energy absorption at lower, non-critical conditions [48,49]. Moreover, n-octadecane exhibited consistent thermal behaviour over 20 consecutive phase change cycles (thermal stability demonstrated also after 100 heating–cooling cycles available in SI), indicating good thermal stability and reliability under repeated use conditions. This prevents sluggish heat transfer and guarantees effective thermal regulation over multiple cycles. Collectively, the combination of high latent heat storage capacity and a phase transition temperature range that aligns with battery safety thresholds makes n-octadecane especially well-suited for BTMS applications [50,51].

Furthermore, the thermal conductivity of n-octadecane was experimentally measured under controlled conditions, yielding a value of 0.15 ± 0.01 W m^{-1} K^{-1} in the liquid state at 33 °C. In the solid state, the thermal conductivity increased markedly to 0.52 ± 0.02 W m^{-1} K^{-1}. These values are consistent with those previously reported in the literature, thereby validating the accuracy of the experimental methodology [29,52,50]. In addition, as illustrated in Fig. 6, the TGA curve shows that the mass loss of n-octadecane begins approximately at 120 °C and all the mass is lost approximately at 220 °C. Therefore, the operational temperature range of n-octadecane should be limited to below 120 °C to prevent evaporation and avoid complete degradation of the material, as supported by literature findings [51,53]. Accordingly, its thermal performance was experimentally evaluated, as detailed in Section 3.2.

3.2. N-octadecane charging and discharging cycles at different HTF volume flow rates

The in-house TES system was utilized to experimentally investigate the thermal response of n-octadecane under varying HTF volume flow rates. Fig. 7 presents the baseline case, in which a flow rate of 2 L min^{-1} of water alone was circulated through the TES system prior to the introduction of PCM. In this baseline assessment, the HTF temperature was increased from 15 °C to 35 °C to quantify the heat exchanged by the system in the absence of PCM.

Fig. 8 illustrated the PCM temperature evolution during charging (a) and discharging (b) cycles at 2 L min^{-1} (Case 1). Similar trends (provided in the Supporting Information) were observed at higher HTF volume flow rate of 2.5 L min^{-1} (Case 2) and 3 L min^{-1} (Case 3), respectively.

At higher flow rates, the temperature gradient across the TES unit slightly reduced, resulting in faster phase change completion and improved thermal uniformity across the PCM volume. As expected, the phase change front advanced from the inlet toward the outlet regions of the TES (Fig. 8.a). During the charging cycle, the PCM adjacent to the top sensor (T9) exhibited the earliest temperature rise and phase transition, followed sequentially by the mid-depth sensors (T3-T7) and the bottom sensor (T8). This stratified response is attributed to the top-to-bottom heat propagation driven by the HTF flow and the presence of aluminum fins, which enhanced heat conduction in the upper and central PCM regions. Particularly, PCM mid-point bottom sensor (T8) exhibited a delayed response in reaching the set point temperature compared to the others due to limited heat transfer rate in proximity to the bottom of the tank, under the aluminium fins. The incorporation of aluminum fins significantly enhances thermal conductivity within the TES system, facilitating more uniform heat distribution and promoting deeper heat penetration into the PCM. This results in an accelerated melting process and a more rapid progression of the melting front [54,55].

In fact, heat conduction mechanism mostly influenced the solid region and played a major role in the initial stages of melting. When the majority of the PCM is in the solid state, its low thermal conductivity results in a high conductive thermal resistance, which becomes the dominant factor governing the overall heat transfer processes. Although varying the volume flow rate alters the forced convection heat transfer coefficient within the copper pipe, this change has a negligible effect on the total heat transfer, as the conductive resistance within the solid PCM remains the primary limiting factor. The buoyancy-driven flow induced by temperature gradients enhanced heat transfer, particularly in regions where pure conduction was insufficient. This effect was especially

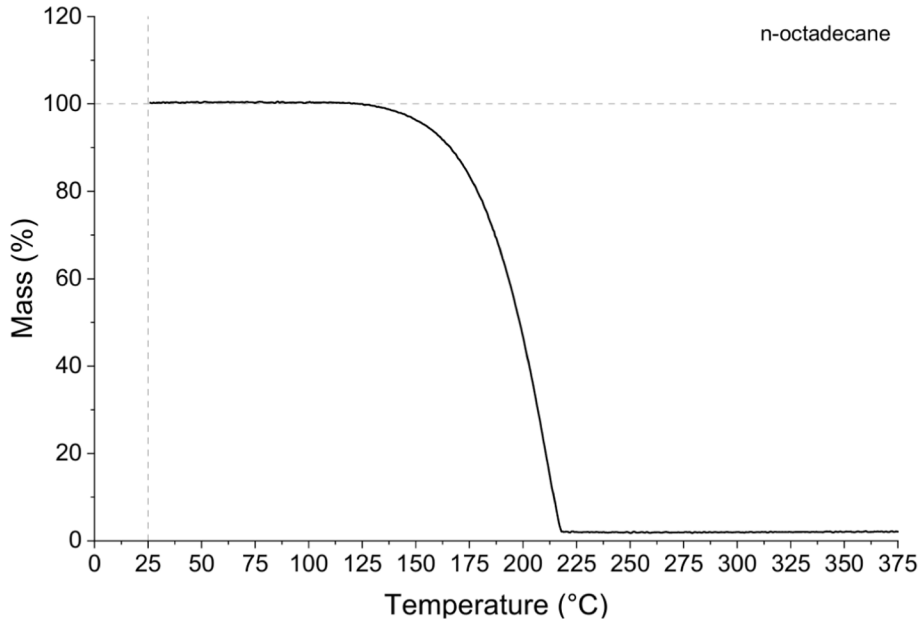

Fig. 6. Thermogravimetric curve of pure n-octadecane.

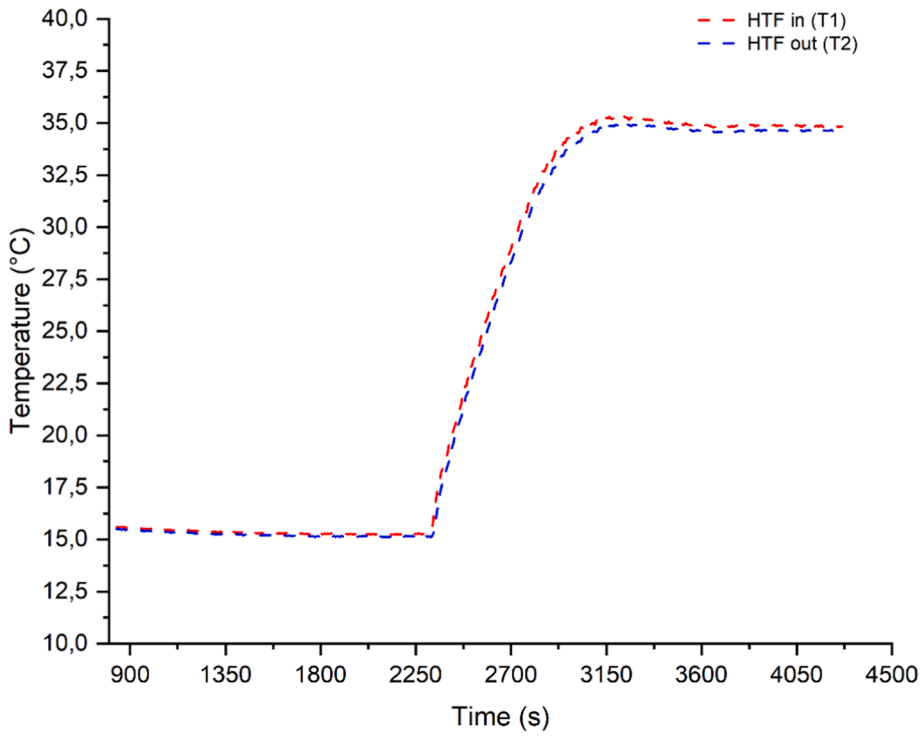

Fig. 7. Baseline case – Test with HTF circulating inside the TES experimental setup without PCM.

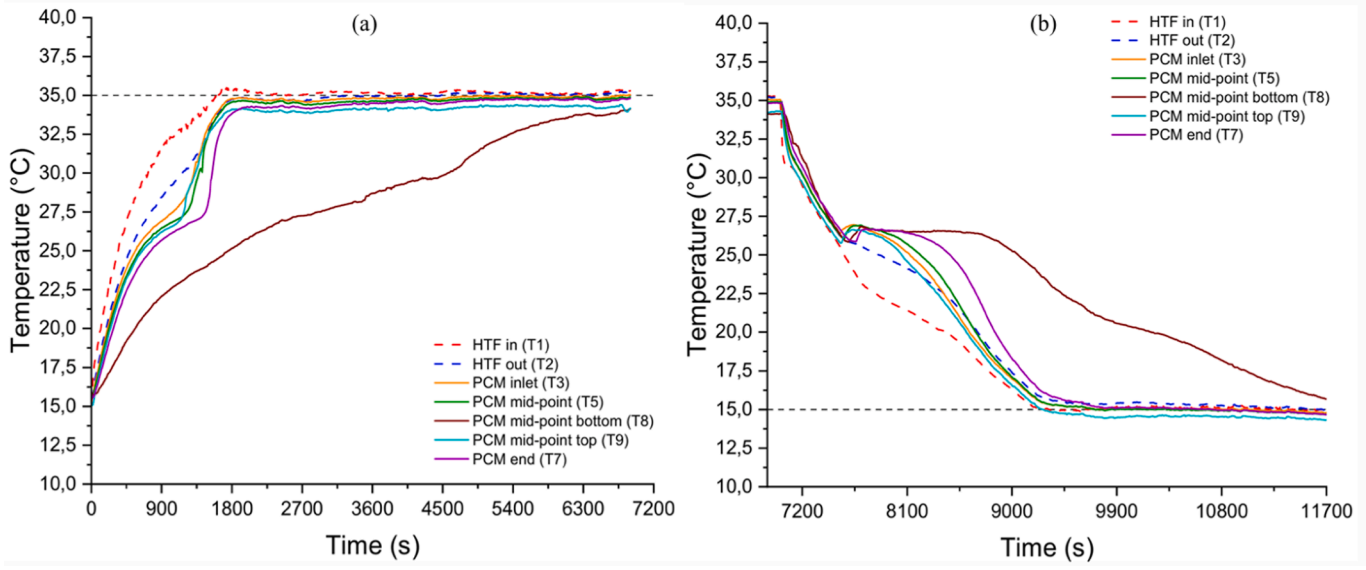

Fig. 8. Temperature vs. time for the TES unit with HTF volume flow rate of 2 L min-1 (Case 1) during the charging (a) and discharging (b) cycle.

pronounced in the lower section of the TES unit, where a slower thermal response was observed.

As the n-octadecane transitioned to a predominantly liquid state, natural convection became the dominant heat transfer mode, effectively controlling the melting process [56]. This transition from conduction- to convection-dominated behaviour can be attributed to the evolution of the melt front and the associated buoyancy-driven flow within the liquid PCM. During the initial melting stage, when the PCM remains predominantly solid, heat transfer occurs primarily through conduction owing to the fixed molecular arrangement and the inherently low thermal conductivity of solid n-octadecane. A thin molten layer first forms adjacent to the heat transfer surface, where temperature gradients are steep and fluid motion is minimal [56]. As the melting front progresses outward, the thickness of this liquid layer increases and density gradients develop in the molten region, initiating buoyancy-driven motion. Warmer, lighter fluid near the heat source rises, while cooler, denser liquid descends, establishing natural convection currents that enhance local heat transport. The strength of natural convection can be quantified using the dimensionless Rayleigh number (Ra), which increases rapidly as the liquid layer thickens and the temperature difference across it grows. This parameter can also be expressed as:

$$Ra = \frac{g\beta\Delta TL^3}{\nu\alpha} = \frac{g\beta\Delta TL^3}{\nu^2} \bullet \frac{\nu}{\alpha} = Gr \bullet Pr \tag{7}$$

Where Gr represents the Grashof number that measures the ratio of buoyancy forces to viscous forces in a fluid and Pr is the Prandtl number,

accounting for thermal diffusion effects (see Table S.1 reported in the Supporting Information for further details). Particularly, when the Rayleigh number exceeds a critical threshold (typically Ra $> 10^4$ for paraffinic PCMs), natural convection becomes substantial, promoting enhanced fluid circulation and increasing the effective thermal conductivity of the molten PCM. In the present analysis, the estimated Rayleigh number is on the order of 10^7, indicating a buoyancy-dominated regime; thus, under the operational conditions considered, natural convection is expected to govern heat transfer within the melted n-octadecane TES. This conduction-to-convection transition explains the experimentally observed acceleration in the melting rate, particularly in the upper and central zones of the TES unit where the liquid layer is thicker and buoyant motion is stronger. In contrast, near the bottom region (T8), the delayed temperature response is attributed to a smaller liquid fraction and weaker buoyancy effects, which limit the onset of convection and maintain conduction as the prevailing mechanism for a longer period. Hence, the spatially stratified temperature evolution observed during the charging process reflects the interplay between conduction in the solid phase and natural convection in the liquid phase. The gradual transition between these regimes governs the overall heat transfer performance of the n-octadecane-based TES, consistent with previously reported findings for paraffinic PCMs [57,58].

At this stage, increasing the HTF flow rate, which raises the forced convection heat transfer coefficient within the copper pipe, begins to contribute meaningfully to the overall heat transfer process. As a result, higher HTF flow rates lead to increased heat transfer rates and a moderately accelerated melting of the PCM [59].

Comparable behaviour was observed during both the charging and discharging cycles across all three experiments conducted under varying HTF volume flow rates. This was mainly attributed to the turbulent flow regime (Reynolds number $>$ 4000) achieved at HTF flow rates exceeding 1 L min^{-1}. Turbulent flow enhances mixing and increases the convective heat transfer coefficient between the HTF and the heat exchanger surface in contact with the PCM. As a result, the higher heat transfer rate speeds up the thermal energy delivery to the PCM and reduces thermal resistance at the interface resulting in faster initiation and propagation of the melting front. Furthermore, turbulence mitigates thermal stratification by promoting uniform temperature distribution throughout the tank, thereby facilitating consistent heat transfer across the entire PCM volume, especially where stagnant zones might otherwise slow the process [60–62]. Nevertheless, Case 3 exhibited a marginally higher charging rate compared to the other cases, primarily due to a reduced temperature gradient between the inlet and outlet of the HTF during the melting phase of n-octadecane. During the discharging process (Fig. 8. b), the rates of discharge remained nearly identical across all three cases, prior to the onset of solidification (from 35 °C to 25 °C). Once the PCM began to solidify, the case with the higher HTF volume flow rate demonstrated a slightly enhanced discharge rate, owing to improved heat transfer performance facilitated by increased convective heat transfer [63]. A similar thermal response was observed during the discharging process, wherein the solidification front initiated at the uppermost region (T9) and advanced downward, with the bottom region (T8). The early formation of a solid PCM layer near the HTF inlet contributed to increased thermal resistance at the heat exchanger interface, which impeded further heat extraction from the lower PCM layers. As the PCM transitioned to a predominantly solid state, the suppression of natural convection further limited heat transfer, particularly in the bottom zone where conduction became the prevailing mechanism. Although increasing the HTF flow rate resulted in improved convective heat transfer and turbulence near the copper tubes, its influence on accelerating solidification at greater depths was marginal. These results highlight the influence of thermocouple position and local heat transfer regimes on phase change kinetics. The consistently delayed thermal response at the bottom sensor (T8) underscores the need for advanced design strategies. Potential improvements include optimize fin geometry, enhanced axial heat conduction pathways, or incorporation of high-conductivity composite materials. Such design optimizations are essential to ensure more uniform phase transition dynamics and to maximize the overall thermal performance of PCM-based TES systems.

3.3. N-octadecane charging and discharging cycles varying the HTF inlet heating temperature

Fig. 9 depicted the temporal evolution of PCM temperature during the charging (a) and discharging (b) cycles at 2 L min^{-1}, under varying the HTF inlet temperature for the melting phase (Case 4).

An increase in the HTF inlet temperature enhances the thermal gradient between the HTF and the PCM, thereby strengthening the heat transfer driving potential and accelerating the charging process, as observed in Fig. 8 (a). Consistent with previous observations, the PCM near the uppermost thermocouple (T9) exhibited the earliest temperature rise and initiation of phase change, followed sequentially by the sensors located at intermediate depths (T3-T7), and finally by the bottom sensor (T8). This thermal response reflects a top-to-bottom heat propagation pattern, primarily governed by the direction of HTF flow and increased by the presence of aluminium fins, which improved thermal conductivity in the upper and middle PCM layers. Conversely, the discharging (Fig. 8 (b)) is noticeably slower compared to Case 1 since the starting temperature for solidification is higher (40 °C). This limited thermal gradient delays the onset and progression of the solidification front, particularly in the lower regions of the storage unit. As a result, the release of latent heat is less efficient, prolonging the discharging cycle and reducing the overall thermal discharge rate.

3.4. Mean power and time comparison at different HTF volume flow rates

Fig. 10 depicted the average thermal power vs. time exchanged during charging (a) and discharging (b) cycles. Table 4 reported the mean thermal power calculated during the charging and discharging of the PCM and the duration of both processes. As presented in Fig. 10 (a) the average thermal power increased from approximately 238 W at 2 L min^{-1} to 264 W at 3 L min^{-1} during charging phase. As the flow rate increases, the PCM temperature rises more rapidly, leading to a greater portion of n-octadecane melted in a shorter duration. This results in a higher amount of latent heat stored by the end of charging process [64].

Mean power of discharging Fig. 10 (b) was slightly lower due to reduced temperature gradients and phase change hysteresis in the solidification process. As the n-octadecane solidifies, a thermal boundary layer forms at the heat exchanger surface, increasing thermal resistance and decreasing the temperature gradient between the PCM and the HTF. Moreover, PCM exhibited a temperature difference between melting and solidification point, resulting in a lower temperature during solidification compared to melting with a consequent reduction of the driving force for heat transfer during the discharging phase as confirmed in literature studies [65,66]. As highlighted in Table 4, Case 3 achieved an average discharging power of 147.98 W, which is 16 % higher than that of Case 1. It is noteworthy that the thermal power ratio in Case 3 was found to be 56 (approximately 4.7 % higher compared to Case 1). Consequently, the increased HTF volume flow rate enhanced the heat transfer mechanisms, leading to an improvement in the thermal system efficiency, despite its limited influence on both the charging and discharging time.

Table 5 summarizes the main outcomes of this study. The experimental results demonstrated that incorporating PCM into the TES system enhanced the gravimetric specific power to 0.056 kW kg^{-1} – 3.5 times higher than the baseline configuration without PCM (0.016 kW kg^{-1}). Similarly, the volumetric specific power reached approximately 68 kW m^3, representing a 6-fold improvement over the baseline case. Both gravimetric and volumetric performance indexes were calculated based on the average power output of the PCM-based TES system during the charging cycle with HTF flow rate of 2 L min^{-1}, considering the overall weight and volume of the TES system, excluding the HTF inside.

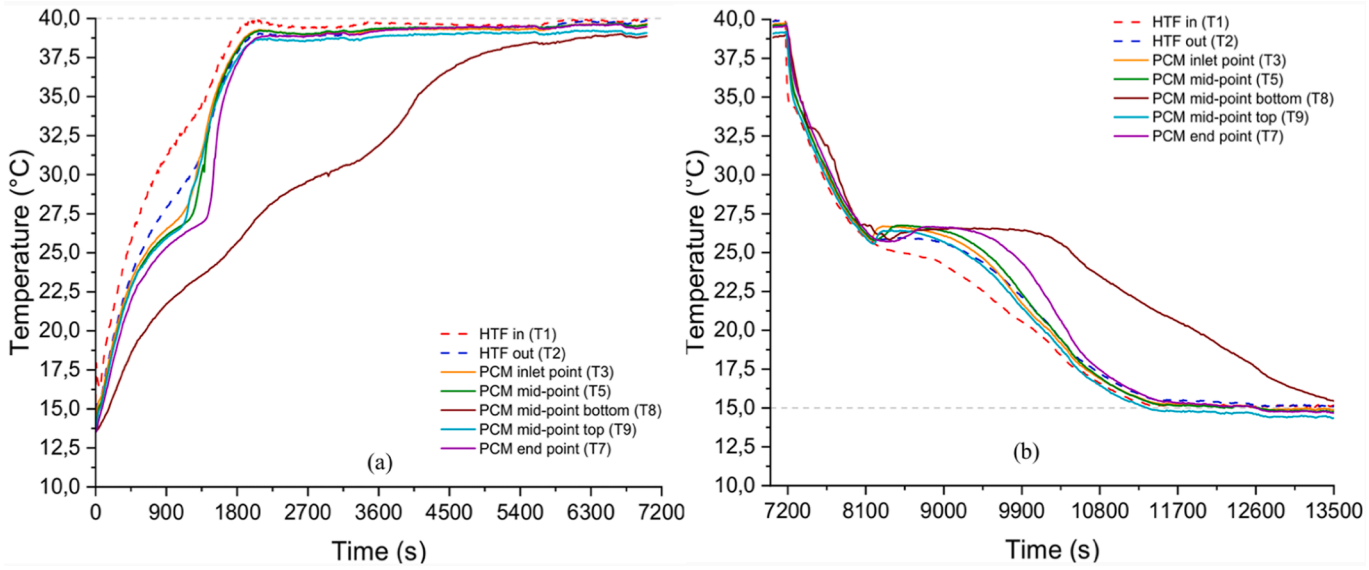

Fig. 9. Temperature vs. time for the TES unit with HTF inlet temperature of 40 °C, flow rate of 2 L min-1 (Case 4) during the charging (a) and discharging (b) cycle.

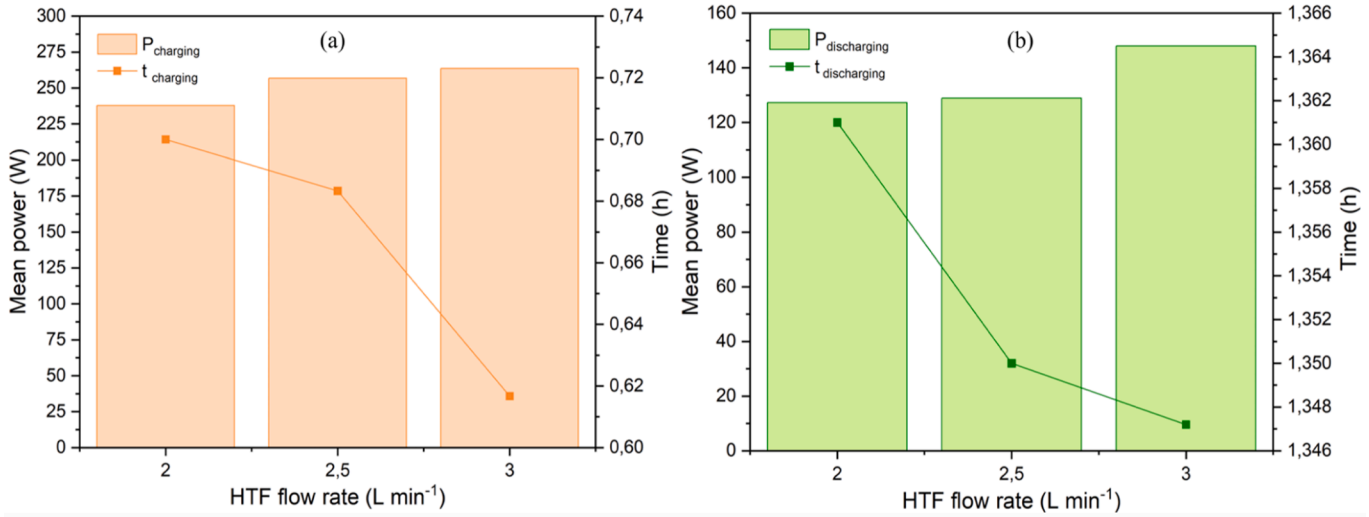

Fig. 10. Mean power of charging vs. time of charging (a) and mean power of discharging vs. time of discharging (b) at different HTF volume flow rate.

Table 4
Results of mean power of charging and discharging cycle vs. time at different HTF volume flow rate.

Case	Mean power of charging	Time of charging	Mean power of discharging	Time of discharging	η_{TES}
1	238 W	2520 s	127 W	4900 s	53.4
2	257 W	2460 s	129 W	4860 s	50.2
3	264 W	2220 s	148 W	4850 s	56.1

Under Case 3 conditions, with a HTF flow rate of 3 L min^{-1}, the specific power exhibited a marginal increase to 0.062 kW kg^{-1} and 75 kW m^{-3}.

To conclude, Fig. S.13 (reported in the Supporting Information), the temperature profile presented compares the experimental results obtained from the PCM-based TMS (brown curve) with the conventional air-cooled LiB battery (blue curve, literature data adapted from [36]). The results clearly indicate that the PCM-assisted configuration effectively limits the maximum temperature below 35 °C throughout the entire discharge–charge cycle. This temperature lies within the recommended operational window for LiB batteries, ensuring stable performance, improved durability, and enhanced safety. As highlighted in Fig. S.13 (b), the latent heat absorbed during the n-octadecane melting phase prevents temperature overshoot, while the subsequent solidification allows gradual heat release. This cyclic heat buffering capability could maintain the battery within its optimal operating range,

Table 5
Major findings of the experimental PCM-based TES system.

Description	Value	Unit
PCM mass	1.96	kg
PCM volume	2.51	L
System overall weight (heat exchanger + casing + PCM)	4.245	kg
System overall volume (excluding insulation layers)	0.0035	m^3
TES gravimetric specific power in baseline case (without PCM)	0.016	kW kg^{-1}
TES volumetric specific power in baseline case (without PCM)	11	kW m^{-3}
TES gravimetric specific power in Case 1 (with PCM)	0.056	kW kg^{-1}
TES volumetric specific power in Case 1 (with PCM)	68	kW m^{-3}
TES gravimetric specific power in Case 3 (with PCM)	0.062	kW kg^{-1}
TES volumetric specific power in Case 3 (with PCM)	75	kW m^{-3}

effectively mitigating the risks observed in air-cooled systems.

4. Conclusions

Thermal management is essential to enable performance, energy efficiency, and long-term durability in HDVs. With the ongoing electrification of powertrains and increasingly stringent emissions regulations, the development of advanced, integrated thermal control systems is becoming indispensable in the design of modern commercial vehicles. BTM is critical in HDVs to ensure safety, reliability, performance, and longevity under the demanding operational conditions typical of HDVs. Particularly, PCMs in HDV battery thermal management offer a promising solution to handle high heat loads passively, improving safety and battery lifespan while complementing active cooling systems. This study presented a comprehensive thermal characterization DSC analysis of various commercial PCMs to identify the most suitable for BTM purpose, based on long-term thermal stability and key thermophysical properties. N-octadecane emerged as the optimal candidate due to its high latent heat capacity and good thermal stability over 20 consecutive thermal cycles. The melting and solidification of n-octadecane, the heat transfer performance, the mean power and thermal power ratio of the PCM-based TES system, together with the influence of HTF volume flow rate variation were experimentally investigated.

Among the valuable insights, n-octadecane, exhibiting a melting range between 25 °C and 32 °C, emerges as a promising PCM for BTMS. DSC analysis reported a latent heat of melting of 222.2 J g^{-1} and a latent heat of solidification of −218.4 J g^{-1}. Charging and discharging tests of n-octadecane at different HTF flow rates were experimentally conducted in a dedicated TES system. Furthermore, in solid state, heat transfer within the PCM is dominated by conduction, as its low thermal conductivity results in high thermal resistance. In liquid state, heat transfer becomes convection-dominated, leading to an enhanced heat transfer rate due to the reduced overall thermal resistance of the PCM. In particular, the PCM temperature sensor located at the mid-point bottom of the storage unit recorded a slower melting rate compared to the central and top thermocouples. This behaviour is attributed to the lower heat transfer efficiency beneath the aluminium fins, which limited the advancement of the melting front in that region. This further emphasizes the importance of minimizing the thermal path between the PCM and the fins within the TES unit to optimize heat transfer efficiency. The effect of varying the HTF volume flow rate is not remarkable, resulting in small changes both in the mean power of charging and discharging evaluated. This could be mainly attribute to the turbulent regime of each experimental test. At high HTF flow rate of 3 L min^{-1} (Case 3) resulted in a thermal power ratio of 56, marking an approximate 4.7 % increase compared to the low flow rate of 2 L min^{-1} (Case 1). Although the increased HTF flow rate had a limited effect on charging and discharging durations, it effectively enhanced the heat transfer processes, thereby contributing to improved overall system performance. Experimental findings confirmed that the incorporation of PCM into the TES system increased the TES gravimetric specific power to 0.056 kW kg^{-1}, representing a 3.5-fold enhancement over the baseline configuration without PCM, which achieved 0.016 kW kg^{-1}. In addition, the volumetric specific power improved to approximately 68 kW m^{-3} – 6 times higher than the baseline.

The findings of this study provide a foundation for the design and optimization of PCM-integrated TES system for BTMS applications. Employing a modular approach, the PCM-TES can be effectively adapted as a versatile and scalable solution for integration into larger-scale systems, including battery pack cooling or EVs cabin heat management. Future studies will be devoted to improving the performance of the TES system to overcome the actual limitations in practical applications. Enhancing the thermal performance of pure PCMs requires a synergistic blend of structural innovation, material augmentation, and phase-change control. Novel heat-exchanger designs — such as finned geometries, metal-foam matrices, and eccentric configurations — significantly enhances heat transfer rates, reducing melting and solidification time [67]. Simultaneously, embedding high-conductivity additives including nanoparticles, expanded graphite, or composite media — can boost effective thermal conductivity several-fold while preserving latent heat storage [68]. Finally, a deeper grasp of phase-change dynamics—mitigating supercooling and phase segregation, and managing nucleation kinetics — ensures repeatable, efficient cycling in practical systems [69,70].

CRediT authorship contribution statement

Elisa Revello: Writing – original draft, Methodology, Investigation, Formal analysis, Conceptualization. **Prakhar Dixit:** Writing – review & editing, Formal analysis, Data curation. **Konsta Turunen:** Formal analysis, Data curation. **Annukka Santasalo-Aarnio:** Writing – review & editing, Supervision, Funding acquisition, Data curation, Conceptualization. **Alessandro Hugo Antonio Monteverde:** .

Declaration of competing interest

The authors declare that they have no known competing financial interests or personal relationships that could have appeared to influence the work reported in this paper.

Acknowledgments

This work was funded by the NextGeneration EU 2022 Research and Innovation programme under DM 352 (CUP No E12B22000520006) within the National Recovery and Resilience Plan (PNRR), and by Leonardo S.p.A through the funding of E. Revello's doctoral scholarships. The authors would like to thank the institution Politecnico di Torino and Ministry of University and Research (MUR) for providing this opportunity. Furthermore, the authors would also express their gratitude to Professor A. Santasalo-Aarnio for the hosting period at Aalto University and to all staff members of the Energy Conversion and System Group for their valuable support during the experimental phase. The authors wish to acknowledge also Senior Scientist Ari Seppälä for the thermal conductivity measurements conducted. Additional financial support was provided by the Research council of Finland through the project THERMAMAZE (363655).

Appendix A. Supplementary data

Supplementary data to this article can be found online at https://doi.org/10.1016/j.enconman.2025.120816.

Data availability

Data will be made available on request.

References

[1] Campanari S, Manzolini G, Garcia de la Iglesia F. Energy analysis of electric vehicles using batteries or fuel cells through well-to-wheel driving cycle simulations. J Power Sources 2009;186:464–77. https://doi.org/10.1016/j.jpowsour.2008.09.115.
[2] Wazeer A, Das A, Abeykoon C, Sinha A, Karmakar A. Phase change materials for battery thermal management of electric and hybrid vehicles: a review. Energy Nexus 2022;7. https://doi.org/10.1016/j.nexus.2022.100131.
[3] IEA n.d. https://www.iea.org/energy-system/transport/trucks-and-buses (accessed May 14, 2025).
[4] Manzetti S, Mariasiu F. Electric vehicle battery technologies: from present state to future systems. Renew Sustain Energy Rev 2015;51:1004–12. https://doi.org/10.1016/j.rser.2015.07.010.
[5] Hannan MA, Lipu MSH, Hussain A, Mohamed A. A review of lithium-ion battery state of charge estimation and management system in electric vehicle applications: challenges and recommendations. Renew Sustain Energy Rev 2017;78:834–54. https://doi.org/10.1016/j.rser.2017.05.001.

[6] Hasan MM, Haque R, Jahirul MI, Rasul MG, Fattah IMR, Hassan NMS, et al. Advancing energy storage: the future trajectory of lithium-ion battery technologies. J Energy Storage 2025;120. https://doi.org/10.1016/j.est.2025.116511.

[7] Safari M. Battery electric vehicles: looking behind to move forward. Energy Policy 2018;115:54–65. https://doi.org/10.1016/j.enpol.2017.12.053.

[8] Previati G, Mastinu G, Gobbi M. Thermal Management of Electrified Vehicles—A Review. Energies (Basel) 2022;15. https://doi.org/10.3390/en15041326.

[9] Li Z, Zhang Y, Zhang S, Tang B. Phase change materials for lithium-ion battery thermal management systems: a review. J Energy Storage 2024;80. https://doi.org/10.1016/j.est.2023.110259.

[10] Huang J, Shoai Naini S, Miller R, Rizzo D, Sebeck K, Shurin S, et al. Development of a heat pipe–based battery thermal management system for hybrid electric vehicles. Proc Inst Mech Eng, Part D: J Automob Eng 2020;234:1532–43. https://doi.org/10.1177/0954407019899588.

[11] Ranjbar Kermani J, Mahlouji Taheri M, Pakzad H, Minaei M, Bijarchi MA, Moosavi A, et al. Hybrid battery thermal management systems based on phase transition processes: a comprehensive review. J Energy Storage 2024;86. https://doi.org/10.1016/j.est.2024.111227.

[12] Xie P, Jin L, Qiao G, Lin C, Barreneche C, Ding Y. Thermal energy storage for electric vehicles at low temperatures: Concepts, systems, devices and materials. Renew Sustain Energy Rev 2022;160. https://doi.org/10.1016/j.rser.2022.112263.

[13] Kuitunen S. Thermal storage based heating system for full electric city buses n.d. https://doi.org/10.13140/RG.2.2.24919.57766.

[14] Sun M, Liu T, Wang X, Liu T, Li M, Chen G, et al. Roles of thermal energy storage technology for carbon neutrality. Carbon Neutrality 2023;2. https://doi.org/10.1007/s43979-023-00052-w.

[15] Sharma A, Tyagi VV, Chen CR, Buddhi D. Review on thermal energy storage with phase change materials and applications. Renew Sustain Energy Rev 2009;13:318–45. https://doi.org/10.1016/j.rser.2007.10.005.

[16] Electric bus range, focus on electricity consumption. A sum-up 2023.

[17] Kraft W, Stahl V, Vetter P. Thermal storage using metallic phase change materials for bus heating-state of the art of electric buses and requirements for the storage system. Energies (Basel) 2020;13. https://doi.org/10.3390/en13113023.

[18] Wang M, Wolfe Edward, Craig Timothy, Laclair TJ, Abdelaziz Omar, Gao Zhiming. Design and Testing of a Thermal Storage System for Electric Vehicle Cabin Heating. 2016.

[19] Hossan MA, Al Deen Aryan S, Noman MSH, Ahmed DH. Phase change material-based rooftop on public transport for thermal management☆. Energy Storage Sav 2023;2:549–58. https://doi.org/10.1016/j.enss.2023.08.001.

[20] Pra F, Al Koussa J, Ludwig S, De Servi CM. Experimental and numerical investigation of the thermal performance of a hybrid battery thermal management system for an electric van. Batteries 2021;7. https://doi.org/10.3390/batteries7020027.

[21] Khateeb SA, Farid MM, Selman JR, Al-Hallaj S. Design and simulation of a lithium-ion battery with a phase change material thermal management system for an electric scooter. J Power Sources 2004;128:292–307. https://doi.org/10.1016/j.jpowsour.2003.09.070.

[22] Zhang J, Li X, He F, He J, Zhong Z, Zhang G. Experimental Investigation on thermal Management of Electric Vehicle Battery Module with Paraffin/Expanded Graphite Composite phase Change Material. Int J Photoenergy 2017; 2017.. https://doi.org/10.1155/2017/2929473.

[23] Wu W, Yang X, Zhang G, Chen K, Wang S. Experimental investigation on the thermal performance of heat pipe-assisted phase change material based battery thermal management system. Energy Convers Manag 2017;138:486–92. https://doi.org/10.1016/j.enconman.2017.02.022.

[24] Kalidasan B, Pandey AK. Next generation phase change materials: State-of-the-art towards sustainable future. Prog Mater Sci 2025;148:101380. https://doi.org/10.1016/J.PMATSCI.2024.101380.

[25] Mehling H. Review and analysis of existing approaches to investigate property degradation of phase change materials and development of a new systematic approach. Appl Sci (Switzerland) 2023;13. https://doi.org/10.3390/app13158682.

[26] Shukla A, Buddhi D, Sawhney RL. Thermal cycling test of few selected inorganic and organic phase change materials. Renew Energy 2008;33:2606–14. https://doi.org/10.1016/j.renene.2008.02.026.

[27] Wadee A, Walker P, McCullen N, Ferrandiz-Mas V. The effect of thermal cycling on the thermal and chemical stability of paraffin phase change materials (PCMs) composites. Mater Struct/Materiaux et Constructions 2025;58. https://doi.org/10.1617/s11527-024-02556-y.

[28] Shank K, Bernat J, Regal E, Leise J, Ji X, Tiari S. Experimental study of varying heat transfer fluid parameters within a latent heat thermal energy storage system enhanced by fins. Sustainability (Switzerland) 2022;14. https://doi.org/10.3390/su14148920.

[29] Faden M, Höhlein S, Wanner J, König-Haagen A, Brüggemann D. Review of thermophysical property data of octadecane for phase-change studies. Materials 2019;12. https://doi.org/10.3390/ma12182974.

[30] Zhang X, Zhu C, Fang G. Preparation and thermal properties of n-eicosane/nano-SiO2/expanded graphite composite phase-change material for thermal energy storage. Mater Chem Phys 2020;240. https://doi.org/10.1016/j.matchemphys.2019.122178.

[31] Wang X, Cheng Q, Wu M, Du P, Liu C, Rao Z. Thermal properties optimization of lauric acid as phase change material with modified boron nitride nanosheets-sodium sulfate for thermal energy storage. J Energy Storage 2023;61:106781. https://doi.org/10.1016/J.EST.2023.106781.

[32] Yazdani MR, Laitinen A, Helaakoski V, Farnas LK, Kukko K, Saari K, et al. Efficient storage and recovery of waste heat by phase change material embedded within additively manufactured grid heat exchangers. Int. J Heat Mass Transf 2021;181. https://doi.org/10.1016/j.ijheatmasstransfer.2021.121846.

[33] Zhu C, Chen Y, Cong R, Ran F, Fang G. Improved thermal properties of stearic acid/high density polyethylene/carbon fiber composite heat storage materials. Sol Energy Mater Sol Cells 2021;219:110782. https://doi.org/10.1016/J.SOLMAT.2020.110782.

[34] Fatahi H, Claverie J, Poncet S. Thermal characterization of phase change materials by differential scanning calorimetry: a Review. Appl Sci (Switzerland) 2022;12. https://doi.org/10.3390/app122312019.

[35] Gao M, Zhao S, Yang H, Wu X, Xiao Y. An Analysis of the Influence of DSC Parameters on the Measurement of the thermal Properties of Phase-Change Material. Materials 2024;17. https://doi.org/10.3390/ma17235689.

[36] Jiang ZY, Qu ZG. Lithium–ion battery thermal management using heat pipe and phase change material during discharge–charge cycle: a comprehensive numerical study. Appl Energy 2019;242:378–92. https://doi.org/10.1016/j.apenergy.2019.03.043.

[37] Liquid water density as function of temperature and pressure n.d. https://www.engineeringtoolbox.com/water-density-specific-weight-d_595.html (accessed May 27, 2025).

[38] Isobaric heat capacity of water as function of temperature n.d. https://www.engineeringtoolbox.com/specific-heat-capacity-water-d_660.html (accessed May 27, 2025).

[39] Li L, Yu H, Wang X, Zheng S. Thermal analysis of melting and freezing processes of phase change materials (PCMs) based on dynamic DSC test. Energ Buildings 2016;130:388–96. https://doi.org/10.1016/J.ENBUILD.2016.08.058.

[40] Rathod MK, Banerjee J. Thermal stability of phase change materials used in latent heat energy storage systems: a review. Renew Sustain Energy Rev 2013;18:246–58. https://doi.org/10.1016/j.rser.2012.10.022.

[41] Zhu C, Chen Y, Cong R, Ran F, Fang G. Improved thermal properties of stearic acid/high density polyethylene/carbon fiber composite heat storage materials. Sol Energy Mater Sol Cells 2021;219. https://doi.org/10.1016/j.solmat.2020.110782.

[42] Kumarasamy K, An J, Yang J, Yang EH. Numerical techniques to model conduction dominant phase change systems: a CFD approach and validation with DSC curve. Energ Buildings 2016;118:240–8. https://doi.org/10.1016/j.enbuild.2016.02.040.

[43] Hussein MZ, Zainal Z. Properties of N-Octadecane-encapsulated activated carbon nanocomposite for energy storage medium: the effect of surface area and pore structure. 2015.

[44] Maithya OM, Li X, Feng X, Sui X, Wang B. Microencapsulated phase change material via Pickering emulsion stabilized by graphene oxide for photothermal conversion. J Mater Sci 2020;55:7731–42. https://doi.org/10.1007/s10853-020-04499-5.

[45] Ma G, Han L, Sun J, Jia Y. Thermal properties and reliability of eutectic mixture of stearic acid-acetamide as phase change material for latent heat storage. J Chem Thermodyn 2017;106:178–86. https://doi.org/10.1016/j.jct.2016.11.022.

[46] Zhang K, Wang J, Xu L, Xie H, Guo Z. Preparation and thermal characterization of n-octadecane/pentafluorostyrene nanocapsules for phase-change energy storage. J Energy Storage 2021;35:102327. https://doi.org/10.1016/J.EST.2021.102327.

[47] Xu L, Yang R. Stearic acid/inorganic porous matrix phase change composite for hot water systems. Molecules 2019;24. https://doi.org/10.3390/molecules24081482.

[48] Malik M, Dincer I, Rosen MA. Review on use of phase change materials in battery thermal management for electric and hybrid electric vehicles. Int J Energy Res 2016;40:1011–31. https://doi.org/10.1002/er.3496.

[49] Fu P, Zhao L, Wang X, Sun J, Xin Z. A Review of Cooling Technologies in Lithium-Ion Power Battery Thermal Management Systems for New Energy Vehicles. Processes 2023;11. https://doi.org/10.3390/pr11123450.

[50] Cao S, Zhao X, Wang F, Wang J, Yang R. Experimental investigation on the thermophysical properties and solidification characteristics of n-octadecane in a spherical capsule. Case Stud Therm Eng 2024;64. https://doi.org/10.1016/j.csite.2024.105475.

[51] Lin L, Li Z, Zhang J, Ma T, Wei R, Zhang Q, et al. MUF-n-Octadecane phase-change microcapsules: effects of core pH and core–wall ratio on morphology and thermal properties of microcapsules. Molecules 2024;29. https://doi.org/10.3390/molecules29204794.

[52] Harish S, Ishikawa K, Chiashi S, Shiomi J, Maruyama S. Anomalous thermal conduction characteristics of phase change composites with single-walled carbon nanotube inclusions. J Phys Chem C 2013;117:15409–13. https://doi.org/10.1021/jp4046512.

[53] Li C, Ni L, Chen Q, Jiang J, Zhou K. Temperature control of exothermic reactions using n-Octadecane@MF Resin microPCMs based on esterification reactions. Processes 2022;10. https://doi.org/10.3390/pr10020239.

[54] Yu M, Sun X, Su W, Li D, Shen J, Zhang X, et al. Investigation on the melting performance of a phase change material based on a shell-and-tube thermal energy storage unit with a rectangular fin configuration. Energies (Basel) 2022;15. https://doi.org/10.3390/en15218200.

[55] Ye W, Jamshideasli D, Khodadadi JM. Improved performance of latent heat energy storage systems in response to utilization of high thermal conductivity fins. Energies (Basel) 2023;16. https://doi.org/10.3390/en16031277.

[56] Uddin M, Virk ASU, Park C. Natural convection in the melting of phase change materials in a cylindrical thermal energy storage system: effects of flow arrangements of heat transfer fluid and associated thermal boundary conditions. J Therm Sci Eng Appl 2023;15. https://doi.org/10.1115/1.4063045.

[57] Alva G, Lin Y, Fang G. An overview of thermal energy storage systems. Energy 2018;144:341–78. https://doi.org/10.1016/j.energy.2017.12.037.

[58] Kamkari B, Shokouhmand H. Experimental investigation of phase change material melting in rectangular enclosures with horizontal partial fins. Int J Heat Mass Transf 2014;78:839–51. https://doi.org/10.1016/J.IJHEATMASSTRANSFER.2014.07.056.
[59] Liu C, Groulx D. Experimental study of the phase change heat transfer inside a horizontal cylindrical latent heat energy storage system. Int J Therm Sci 2014;82:100–10. https://doi.org/10.1016/j.ijthermalsci.2014.03.014.
[60] Xiong T, Wang Y, Yang X. Numerical investigation of dynamic melting process in a thermal energy storage system using U-tube heat exchanger. Adv Mech Eng 2017;9. https://doi.org/10.1177/1687814017707415.
[61] Riahi S, Saman WY, Bruno F, Tay NHS. Numerical study of melting process of a high-temperature phase change material including natural convection and turbulence. Int J Comput Meth Experiment Measure 2017;5:723–32. https://doi.org/10.2495/CMEM-V5-N5-723-732.
[62] Khalaf AF, Rashid FL, Letif SA, Ameen A, Mohammed HI. A numerical study of the effect of water speed on the melting process of phase change materials inside a vertical cylindrical container. Appl Sci (Switzerland) 2024;14. https://doi.org/10.3390/app14083212.
[63] Sadiq IE, Aljabair S, Karamallah AA. Accelerated solidification of PCM via Al2O3/CuO hybrid nanoparticles in triplex tube heat storage. J Thermal Eng 2024;10:880–903. https://doi.org/10.14744/thermal.0000838.
[64] Javadi FS, Metselaar HSC, Ganesan PB. Experimental Investigation on Prototype Latent Heat thermal Battery Charging and Discharging Function Integrated with Solar Collector. Energ Eng: J Ass Energ Eng 2022;119:1587–610. https://doi.org/10.32604/ee.2022.020304.
[65] Lu D, Xu X, Zhang X, Xie W, Gao Y. Study on influencing factors of phase transition hysteresis in the phase change energy storage. Materials 2022;15. https://doi.org/10.3390/ma15082775.
[66] Fadl M, Eames P. Thermal performance analysis of the charging/discharging process of a shell and horizontally oriented multi-tube latent heat storage system. Energies (Basel) 2020;13. https://doi.org/10.3390/en13236193.
[67] Ghalambaz M, Mehryan SAM, Ayoubloo KA, Hajjar A, El KM, Younis O, et al. Thermal energy storage and heat transfer of nano-enhanced phase change material (NePCM) in a shell and tube thermal energy storage (TES) unit with a partial layer of eccentric copper foam. Molecules 2021;26. https://doi.org/10.3390/molecules26051491.
[68] Choure BK, Alam T, Kumar R. A review on heat transfer enhancement techniques for PCM based thermal energy storage system. J Energy Storage 2023;72:108161. https://doi.org/10.1016/J.EST.2023.108161.
[69] Said Z, Pandey AK, Tiwari AK, Kalidasan B, Jamil F, Thakur AK, et al. Nano-enhanced phase change materials: Fundamentals and applications. Prog Energy Combust Sci 2024;104. https://doi.org/10.1016/j.pecs.2024.101162.
[70] Liu P, Wu D, Xiong T, Cao X, Tan Z, Lin W, et al. Enhanced thermal Properties of Composite phase Change Material by Polydopamine-Driven Cu Nanoparticles. Energy Mater Adv 2025;6. https://doi.org/10.34133/energymatadv.0183.